Biplane Transrectal Ultrasound Probe Calibration using Dual-arm Robotic System with Multi-DOF End-effectors

Jing Xiong, Member, IEEE, Qiangyun Li, Faizan Ahmad, Changfu Xu, Hao Deng, and
Zeyang Xia*, Senior Member, IEEE

Abstract— Transrectal Ultrasound (TRUS)-guided dual-arm robotic needle insertion system has improved clinical diagnosis treatment for biopsy and brachytherapy. It provides a highly precise and flexible method for inserting surgical needles. In the existing system, both the probe and needle are fixed to the robot's end flange, which prevents the rotation and translation of the TRUS probe and needle from enabling multi-angle scanning and flexible needle insertion. In our previous work, we developed a dual-arm robotic needle insertion system with multi-degree-of-freedom (DOF) end-effectors to address the aforementioned issues. The calibration accuracy of the system directly determines the system's effectiveness. However, existing calibration schemes are challenging to complete the calibration of the dual-arm robotic needle insertion system with multi-DOF end-effectors. Therefore, this paper presents a biplane TRUS probe calibration using dual-arm robotic needle insertion system with multi-DOF end-effectors. In the proposed approach, the kinematic of the multi-DOF probe and needle are first modeled to obtain the calibration parameters. Then the multi-DOF needle and probe are calibrated as the biplane TRUS image, which can be used to track the different motion states of the probe and needle. Finally, the experimental results are obtained and validated on the TRUS-guided dual-arm robotic needle insertion system. The results showed that the calibration accuracy of the overall system is 0.80±0.23 mm, which meets the clinical requirements.

Index Terms Calibration approach, Biplane TRUS, Dual-arm robot, Multi-DOF end-effectors

J. Xiong is with Medical Robotics and Minimally Invasive Surgical Devices, Shenzhen Institute of Advanced Technology, Chinese academy of Sciences, Shenzhen 518055, China (e-mail: jing.xiong@siat.ac.cn).

Q. Li, F. Ahmad, and H. Deng are with Soft Robotics Research Center, Shenzhen Institute of Advanced Technology, and also with University of Chinese Academy of Sciences, Shenzhen 518055, China (e-mails: qy.li1, faizanahmad, hao.deng@siat.ac.cn).

C. Xu is with Soft Robotics Research Center, Shenzhen Institute of Advanced Technology, Chinese academy of Sciences, Shenzhen 518055, China (e-mail: cf.xu@siat.ac.cn).

Z. Xia is with Soft Robotics Research Center, Shenzhen Institute of Advanced Technology, Chinese Academy of Sciences, Shenzhen, 518055, China, and also with the Key Laboratory of Human-Machine Intelligence-Synergy Systems, Shenzhen Institute of Advanced Technology, CAS, Shenzhen 518055, China (e-mail: zy.xia@siat.ac.cn).

I. INTRODUCTION

With the rapid advancement of robot technology, the image-guided robotic needle insertion system was successfully applied, thereby enhancing clinical diagnosis and treatment [1], [2], including biopsy [3], [4], ablation [4], [5], drug delivery [6], and brachytherapy [7], [8]. In recent years, the transrectal ultrasound (TRUS)-guided dual-arm robotic needle insertion system has received much interest to its increased flexibility [9], [10], [11], [12]. However, these systems are incapable of multi-angle omnidirectional probe scanning and flexible needle insertion because the probe and needle are fixed to the robot's end flange [13]. In our previous research [14], we built a TRUS-guided dual-arm robotic needle insertion system with multi-DOF end-effectors. However, the calibration of the needle and probe is vital for the robotic needle insertion system, and their calibration accuracies directly affect the precision and safety of the robot system during surgical procedures.

Numerous calibrating techniques have been presented in the literature [15], [16], [17], [18], [19] . These existing calibration techniques can be roughly classified into two categories: reconstruction-based and phantom-based calibration. In reconstruction-based calibration methods, an artificial object with known geometric properties is often scanned and reconstructed. Boctor et al. [20] proposed a novel closed-form method for ultrasound calibration by integrating the US calibration framework into the AX = XB framework employing a closed-form solution for the AX = XB problem. This method utilized the difference between the reconstructed and known shapes to recalculate calibration parameters. Shen et al. [21] proposed a rapid and automatic calibration approach based on a 3D-printed phantom and an untracked marker to simplify the standard calibration operations. Using a rigid registration between the computer-aided design (CAD) model of the phantom and the phantom US image, this method can quickly determine the calibration solution. In addition, Wang et al. [22] proposed a method for calibrating multiple cooperative robots by formulating the calibration problem as a fundamental problem involving the solution of the matrix equation AXB = YCZ. However, this strategy typically requires accurate initial estimations, which are not always simple or feasible. Initial parameters are vital for TRUS probe calibration, as they enhance image quality, ensure correct

probe positioning, standardize the process, prioritize patient safety and comfort, and facilitate device compatibility. To address this issue, Ma et al. [23] developed an additional probabilistic method for solving the AXB = YCZ calibration problem without a prior knowledge of the data temporal relationship. However, with these existing methods, an external tracker, such as a camera, is required, which may result in accumulative calibration errors.

In phantom-based calibration methods, fiducials in the phantom were imaged by scanning the probe at different angles, and wire phantoms and flat surface phantoms were frequently utilized. To increase the calibration accuracy, Carbajal et al. [24] proposed an improved N-wire phantom freehand US calibration method based on the middle wires. Kim et al. [25] used a planar surface mockup as a phantom to increase image quality; however, the mockup introduced additional errors. Subsequently, Najafi et al. [26] introduced a multi-wedge phantom calibration method to further enhance the accuracy of calibration. This method solved the calibration matrix using a closed-form solution, allowing for straightforward, rapid, and precise US calibration. In addition, inspired by Carbajal et al. [24], Shen et al. [27] recently developed a unique method for performing probe calibration that considered all wires and yielded superior results. Xiong et al. [14] proposed a mechanism-image fusion strategy to improve the calibration accuracy of an ultrasound-guided dual-arm robotic brachytherapy system. The needle tip location was calibrated by the mechanism localization, and the probe was calibrated by ultrasonic imaging of the needle tip.

These existing calibration methods can only calibrate the probe and needle mounted to the end flange of the robot, which is insufficient for a dual-arm robotic needle insertion system with multi-DOF end-effectors. In this paper, we proposed a biplane TRUS probe calibration using dual-arm robotic needle insertion system with multi-DOF end-effectors. In this method, the kinematic analysis of multi-DOF end-effectors was carried out. Based on the various motion states of the end-effector, the calibration parameters are separated into initial and motion parameters. The initial and motion parameters were calibrated using a TRUS biplane image to follow the various motion states of the needle and probe. Experiments on the TRUS probe using dual-arm robotic needle insertion system with multi-DOF end-effectors were conducted to validate the efficiency of the proposed method.

The rest of the paper is organized as follows: Section II describes the kinematics of the needle and TRUS probe. In section III, the proposed image-based biplane calibration method will be explained. Finally, section IV explains the experimental results and validation of the proposed method.
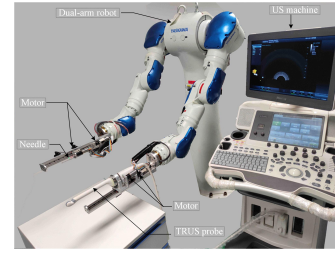

Fig. 1. The TRUS-guided dual-arm robot needle insertion system.

II. System and Kinematics

A. TRUS-guided Dual-arm Robotic Needle Insertion System

The TRUS probe-guided dual-arm robotic needle insertion system consists of a dual-arm robot (YASKAWA SDA10F), a US machine (Mindray DC-8) with a biplane TRUS probe, and two end-effectors. The schematic of the system is shown in Fig. 1.

The end-effectors are essential parts of the system, installed on the dual-arm robot left and right end flanges, respectively. The right arm end-effector is equipped with an insertion needle, and the left arm end-effector is equipped with a TRUS probe. The two motors on each arm control the rotation and translation of the needle and TRUS probe, respectively. Both rotation and translation have initial positions. Each motion of the end-effector starts from the initial position and can be reset to its initial position.

B. Kinematics of Needle and TRUS Probe

The coordinates of dual-arm robot consist of $R_{\mathbf{arm}}$ and $L_{\mathbf{arm}}$ which are the right and left end flange of the robot. The base frame $\mathbb{B}$ of the robot is set as a reference frame. The biplane TRUS probe images provides S-plane and T-plane, where S and T plane are perpendicular to each other.

1) Kinematics of needle: Rotating the needle around itself does not change the needle position, so the needle tip position is determined by the needle translation distance d_n. The kinematic equation of needle is as follows:

$$^{\mathbb{B}}P(d_n) = ^{\mathbb{B}}T_{R_{arm}} \cdot {}^{R_{arm}}P(d_n) \qquad (1)$$

Where $^{\mathbb{B}}P(d_n) = {}^{R_{arm}}P(d_n) + v_n \cdot d_n$, in which v_n is the unit direction vector relative to R_{arm} when the needle is translated. The $^{\mathbb{B}}T_{R_{arm}}$ represents the homogeneous transformation matrix from R_{arm} to $\mathbb{B}$, which is obtained from robot operation system (ROS). The $^{R_{arm}}P(0)$ is the position vector of the needle tip relative to R_{arm} when the needle is at initial position, and $^{R_{arm}}P(d_n)$ is the position vector of the needle tip relative to R_{arm} during needle translation motion. The $d_n \cdot {}^{\mathbb{B}}P(d_n)$ is the position vector of the needle tip relative to $\mathbb{B}$ when the needle is translated d_n.

2) Kinematics of TRUS probe: In TRUS, when the probe is rotated, the pixels position is determined by the probe rotation (θ). Similarly, when the probe is translated, the pixels position is determined by the probes translational distance d_p. The kinematic equation of TRUS probe is as follows:

$$^{\mathbb{B}}P(d_p/\theta) =^{\mathbb{B}} T_{L_{arm}}.^{L_{arm}}T_{img}(d_p/\theta).^{img}P \qquad (2)$$

In which,

$$^{L_{arm}}T_{img}(\theta) = \begin{bmatrix} \mathrm{I} & c \\ 0 & 1 \end{bmatrix}.\begin{bmatrix} \mathrm{R}_{arm}(\mathrm{n},\theta) & 0 \\ 0 & 1 \end{bmatrix}.\begin{bmatrix} \mathrm{I} & -c \\ 0 & 1 \end{bmatrix}.^{L_{arm}}T_{img}(d_p,0),$$

$^{L_{arm}}T_{img}(d_p) =^{L_{arm}} T_{img}(0,\theta) + \begin{bmatrix} \mathrm{I} & d_p.v_p \\ 0 & 1 \end{bmatrix}$. where n $=$ n(0)$+d_p.v_p$, and c $=$ c(0)$+d_p.v_p$. v_p is the unit direction vector relative to L$_{\mathbf{arm}}$ during translational movement of probe. The $^{\mathbb{B}}T_{L_{arm}}$ shows homogeneous transformation matrix from L$_{\mathbf{arm}}$ to $\mathbb{B}$, which is obtained by ROS, ^{img}P is pixels position vector relative to image coordinates system (S and T) plane, R(n,0) is the transformation matrix when coordinates system rotates θ in the direction of n, and $^{\mathbb{B}}P(d_p/\theta)$ is the pixels position vector relative to $\mathbb{B}$.

TABLE I shows all the parameters that need to be calibrated according to the kinematics equations (1) and (2). When the needle and probe at initial state, the initial parameters must be calibrated ($^{R_{arm}}P_t(0)$, $^{L_{arm}}T_{img}(0,0)$). The translational (v_n, v_p) and rotational (n(0), c(0)) parameters are needed to be calibrated during translational and rotational motion, respectively.

TABLE I

Calibration parameters

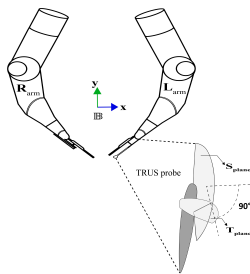| Calibration object | Initial | Motion parameters | |
		Transnational	Rotational
Needle	$^{R_{arm}}P_t(0)$	v_n	-
TRUS probe	$^{L_{arm}}T_{img}(0,0)$	v_p	n(0), c(0)

Fig. 2.   The geometric model of dual-arm robot and TRUS probe.

III. BIPLANE IMAGE-BASED CALIBRATION APPROACH

The proposed calibration framework is shown in Fig.1. Firstly, the initial parameters of the needle are calibrated using multi-point calibration method [28]. Secondly, the calibrated tip biplane TRUS images are used to calibrate

the probe initial parameters. Finally, the biplane TRUS image records the movement trajectories of the needle and the probe and completes the calibration of motion parameters by trajectory fitting.
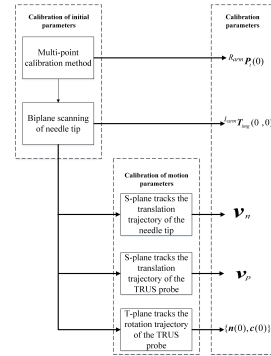

Fig. 3.   Proposed framework of biplane image based calibration for TRUS probe.

A. Calibration of Initial Parameters

1) Needle calibration: The initial parameter $^{R_{arm}}P_t(0)$ refers to the needle-tip coordinates relative to R$_{arm}$, when the needle is at its initial position. To calibrate the needle-tip, we used the multi-point method [28], using equation (3). The procedure are as follows:

$$^{\mathbb{B}}T_{R_{arm}}(i-1).^{R_{arm}}P_t(0) =^{\mathbb{B}} T_{R_{arm}}.^{R_{arm}}P_t(0), i = 1,...,n \qquad (3)$$

Procedure 1: Calibration of needle initial parameters

---

1) Reset the needle to its initial position;
2) Make the needle-tip touch the fixed reference point in different postures, and record $^{\mathbb{B}}T_{R_{arm}}$;
3) Calculate $^{R_{arm}}P_t(0)$ by solving for the least square (LS) [29] using equation (3);

---

2) Probe calibration: The initial parameters $^{L_{arm}}T_{img}(0,0)$ are a set of parameters consisting $^{L_{arm}}T_{S_{img}}(0,0)$ and $^{L_{arm}}T_{T_{img}}(0,0)$. Which represents the homogenous transformation metrics from biplane image coordinates system (S and T) plane to L$_{arm}$ dual arm robotic system when the probe is at initial position. To calibrate $^{L_{arm}}T_{img}(0,0)$, we performed biplane US imaging on the calibrated needle tip using equation (4). The procedures is as follow:

$$^{L_{arm}}T_{img}(0,0) = argmin \sum_{i-1}^{n} ||^{\mathbb{B}}T_{L_{arm}}(i).$$

$$^{L_{arm}}T_{img}(0,0).^{img}P.^{R_{arm}img}P|| \qquad (4)$$

In the above procedures, to calibrate the probe, the needle tip was used instead of the phantom and the robotic system was used instead of the tracker. This eliminates the need for an external position tracker and phantom, thereby reducing costs and avoiding the limitations of their use.

1) Reset the needle and probe to its initial position;
2) Control the robot with a different attitude and allow the TRUS probe scan the calibrated needle tip while the parameters ($^{\mathbb{B}}T_{L_{arm}}(i), {^{\mathbb{B}}T_{R_{arm}}(i)}$) ;
3) Calculate $^{L_{arm}}T_{img}(0,0)$ by solving for the least square (LS) [29] using equation (4);

B. Calibration of Motion Parameters

The motion parameters are composed of translational and rotational parameters. Existing calibration methods were designed for robot needle insertion systems in which both the needle and the probe are fixed on the robot. So they cannot efficiently calibrate the motion parameters. Therefore, we proposed a calibration method to effectively calibrate the motion parameters, which mainly includes two steps: First, the (S and T) plane tracks the translation and rotation trajectories of end-effectors. Second, the calibration of the motion parameters is completed through trajectory fitting.

1) Translational parameters: The calibration parameters v_n and v_p are unit direction vector of needle and probe, respectively. In order to calibrate v_n, we allowed S-plane to track the needle translation trajectory and calculated the coordinates of the trajectory points using equation (5). After that, v_n is calculated by line fitting in 3D space [30]. Similarly, in order to calibrate v_p, we allowed S-plane to track the probe translation trajectory and calculate the coordinates of the trajectory points using equation (6). After that v_p, is calculated by line fitting in 3D space [30]. The calibration procedures are as follows:

$$^{R_{arm}}P(i) = {^{\mathbb{B}}T_{R_{arm}}^{-1}} \cdot {^{\mathbb{B}}T_{L_{arm}}} \cdot {^{L_{arm}}T_{S_{img}}}(0,0) \cdot {^{S_{img}}P(i)} \tag{5}$$

$$^{L_{arm}}P(i) = {^{L_{arm}}T_{S_{img}}}(0,0) \cdot {^{S_{img}}P(i)} \tag{6}$$

Procedure 3: Calibration of needle translational parameters

---

1) Make the needle and probe close to parallel, so that S-plane can scan the needle;
2) The robot behavior is kept unchanged while the parameters $^{\mathbb{B}}T_{L_{arm}}$ and $^{\mathbb{B}}T_{R_{arm}}$ are recorded. The needle is controlled to translate while the S-plane images are saved at different distances. The coordinate $^{S_{img}}P(i)$ of the needle tip in the S-plane can be obtained from the image;
3) The translational locus coordinate $^{R_{arm}}P(i)$ of the needle was calculated by using equation (5);
4) Finally, v_n is calculated by linear fitting to the locus points.;

---

2) Rotational parameters: The calibration parameters $n(0)$ and $c(0)$ are the vectors of center coordinates of the rotated plane relative to L_{arm}, when the TRUS probe at initial position. In order to calibrate the rotational parameters, we allowed T-plane to track the

---

Procedure 4: Calibration of probe translational parameters

---

1) Make the needle and probe close to parallel, so that S-plane can scan the needle;
2) The robot behavior is kept unchanged. The probe is controlled to translate while the S-plane images are saved at different distances. The coordinate $^{S_{img}}P(i)$ of the needle tip in the S-plane can be obtained from the image;
3) The translational locus coordinate $^{R_{arm}}P(i)$ of the probe was calculated by using equation (6);
4) Finally, v_p is calculated by linear fitting to the locus points.;

---

rotational trajectory of the TRUS probe, and calculate the coordinates of the trajectory points using equation (7). After that $n(0)$ and $c(0)$ were calculated using circle fitting in 3D space [31]. The procedure as follows:

$$^{L_{arm}}P(i) = {^{L_{arm}}T_{T_{img}}}(0,0) \cdot {^{T_{img}}P(i)} \tag{7}$$

Procedure 5: Calibration of probe rotational parameters

---

1) Make the needle and probe close to parallel, so that T-plane can scan the needle;
2) The robot behavior is kept unchanged. The TRUS probe is controlled to rotate while the T-plane images are saved at different angles. The coordinate $^{T_{img}}P(i)$ of the intersection point in the T-plane can be obtained from the image;
3) The rotational locus coordinate $^{L_{arm}}P(i)$ of the probe was calculated by using equation (7);
4) Finally, $n(0)$ and $c(0)$ is calculated by circle fitting to the locus points.

IV. EXPERIMENTS AND RESULTS

The proposed method was validated by examining the calibration of the initial and motion parameters and analyzing the system errors on a biplane TRUS-guided dual-arm robot. To assess calibration accuracy, we use mean absolute error (MAE), root square mean error (RMSE), and standard deviation (SD).

$$MAE = \frac{1}{n}\sum_{i-1}^{n}||P_r(i) - P_c(i)|| \tag{8}$$

$$RMSE = \sqrt{\frac{1}{n}\sum_{i-1}^{n}(||P_r(i) - P_c(i)||)^2} \tag{9}$$

$$SD = \sqrt{\frac{1}{n}\sum_{i-1}^{n}(||P_r(i) - \bar{P}_c||)^2} \tag{10}$$

Where n is the number of experiments. The $P_c(i)$ and $P_r(i)$ are the real and calculative position vectors of ith experiment, respectively. The $\bar{P}_c$ is the average value of calculative position vector of n experiments.

A. Evaluation of initial parameters calibration

The procedure of initial parameters calibration is shown in Fig.4. After the calibration of initial parameters, we evaluated the accuracy of needle and probe initial parameters $^{R_{arm}}P_t(0)$ and $^{L_{arm}}T_{img}(0,0)$, respectively. We developed a tip model with precisely known geometric parameters in order to evaluate the calibration accuracy of the needle initial parameter $^{R_{arm}}P_t(0)$. The end-effector of the robot right arm is replaced with tip model and allow the tip-model to touch the reference point as from Fig.5. The geometric parameters are used to calculate the coordinates $^{\mathbb{B}}P_{ref}$ of the reference point relative to $\mathbb{B}$. The coordinates $^{\mathbb{B}}P(0)$ of the reference point relative to $\mathbb{B}$ can also be calculate by the equation (1). The calibration accuracy of the needle initial parameter $^{R_{arm}}P_t(0)$ is calculated using equation (8), (9), and (10). Similarly, to evaluate the calibration accuracy of the probe initial parameters $^{L_{arm}}T_{img}(0,0)$, we collected 10 biplane images of needle tip and calculate the coordinates relative to $\mathbb{B}$ using equation (1) and (3). TABLE II summarizes the accuracy results of initial parameters.
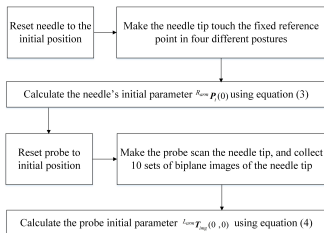

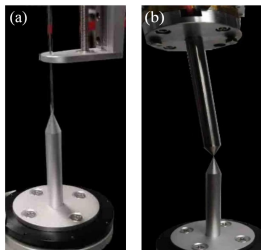Fig. 4. The overall procedure of initial parameters calibration.

Fig. 5. The calibration experimental setups. (a) needle tip touches the fixed reference point; (b) Tip-model touch the reference point.

TABLE II

Calibration Accuracy of Initial Parameters

Initial parameters	Calibration accuracy		
	MAE(mm)	RMSE((mm))	SD(mm)
$^{R_{arm}}P_t(0)$	0.17	0.18	0.03
$^{L_{arm}}T_{Simg}(0,0)$	0.68	0.74	0.29
$^{L_{arm}}T_{Timg}(0,0)$	0.80	0.87	0.36

B. Evaluation of motion parameters calibration

The procedure of motion parameters calibration is shown in Fig.6. After calibration of the motion parameters, we evaluated the accuracy of translation parameters v_n, v_p and rotational parameters $n(0), c(0)$.

To evaluate the calibration accuracy of the translation parameters, the mean distance from the fitting point to the fitting line is specified as the fitting error. In order to determine the accuracy of the translation parameters, the accuracy is measured by the proportion between the distance of the adjacent point and 5 mm. Generally, the proportion is closer to 1 mm, which means the alignment of the image planes is accurate, and the image reconstruction will be reliable and calibration is the more precise. The results are demonstrated in TABLE III. From Fig.7(a), and 7(b), we can visualize the translational trajectory in 3D space and line fitting error of needle and probe, respectively.

To evaluate the calibration accuracy of the rotation parameters, the mean distance from the fitting point to the fitting circle is defined as the fitting error. In order to determine the accuracy of the rotational parameters, the accuracy is measured by the proportion between the center angle of the adjacent point of 3°. Generally, the proportion is closer to 1°, the more precise the calibration. The results are demonstrated in TABLE III. Also, from Fig.7(c), we can visualize the rotational trajectory in 3D space and circle fitting error of probe.

C. Experiment of System Error Analysis

After calibrating initial and motion parameters, we performed system error analysis on four different motion states of the robot: 1) Needle translation state: The needle was translated from 0 to 55 mm; The TRUS probe was at initial position; US images of the needle tip were collected in every 5 mm. 2) Probe translation state: The needle was in the initial position; The TRUS probe was translated from 0 to 65 mm; US images of the needle tip were collected in every 5 mm. 3) Probe rotation state: The needle was in the initial position; The TRUS probe was rotated from $-48°$ to $48°$; US images of the needle tip were collected in every 3°. 4) Totally state: The needle was translated by 5 mm; The TRUS probe was rotated by 3°; The TRUS probe was translated from 0 to 45 mm; US images of the needle tip were collected in every 5 mm. The coordinates of the needle tip relative to $\mathbb{B}$ can be calculated using equation (1) and (2). The distance between the two coordinates are the systematic error, which are demonstrated in TABLE IV.

We recorded MAE, RMSE, and SD of the system error of 0.75 mm, 0.84 mm, and 0.41 mm, and 0.42 mm, 0.48 mm, 0.24 mm for needle and probe, respectively. Similarly, during probe rotation and totally state, we recorded MAE, RMSE, and SD of the system error of 0.30 mm, 0.30 mm, and 0.04 mm, and 0.80 mm, 0.83 mm, 0.23 mm, respectively. Results showed that the calibration accuracy of the overall system was 0.80

TABLE III

Calibration Accuracy of Motion Parameters

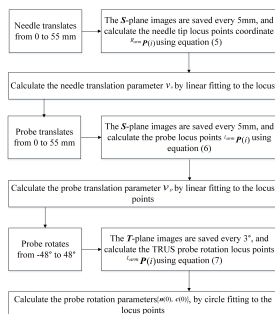| Motion parameters	Fitting error (mm)	Proportion
v_n	0.11	1.00
V_p	0.15	1.03
$n(0), c(0)$	0.02	1.00

Fig. 6.   The overall procedure of motion parameter calibration.

TABLE IV

Systematic error analysis

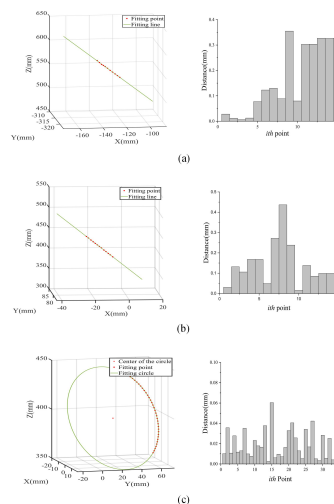|	System error		
Motion states	MAE(mm)	RMSE((mm))	SD(mm)
Needle translation	0.75	0.84	0.41
Probe translation	0.42	0.48	0.24
Probe rotation	0.30	0.30	0.04
Totally state	0.80	0.83	0.23

Fig. 7.   (a) Line fitting of needle translation trajectory in 3D space (Left), line fitting error (Right), (b) Line fitting of probe translation trajectory in 3D space (Left), line fitting error (Right), (c) Circle fitting of probe rotation trajectory in 3D space (Left), circle fitting error (Right).

± 0.23 mm, which is significant in comparison to a clinical accuracy requirement of 2 mm for biopsy and brachytherapy [32]. The MAE and RMSE values of totally state and needle translation are closed to each other. Their relationship is not directly related, but for accurate calibration it is crucial that both the parameters should be closed enough for TRUS-guided procedures.

V. Discussion

In this paper, we proposed a calibration approach based on biplane TRUS probe using dual-arm robotic needle insertion system with multi-DOF end-effectors. This study aims to determine how well the proposed needle and probe calibration system works within a robotic needle insertion system with multi-DOF end-effectors. The results showed that the calibration accuracy of the overall robotic needle insertion system was significantly high (0.80±0.23mm). It is foremost because the biplane TRUS image can be used to track the various motion states of the probe and needle. Therefore, the needle and probe with multi-DOF can be calibrated without an external tracker and complex phantom. Consequently, the errors of these external devices were not accumulating. As a result, the proposed approach can accomplish the needle and probe calibration of the dual-arm robotic needle insertion system with multi-DOF end-effectors while achieving high calibration accuracy.

However, existing calibration methods were only helpful in calibrating the probe and needle attached to the robot end- flange, and they frequently needed an external tracking system and phantom. Therefore, these existing calibration methods cannot be used to calibrate the needle and probe of dual-arm robotic needle insertion systems with multi-DOF end-effectors with a high calibration accuracy. Nevertheless, these methods cannot be used for the needle and probe calibration of dual-arm robotic needle insertion system with multi-DOF end-effectors, and errors were accumulated since an external tracker and complex phantom were used. In contrast, the proposed approach used the biplane image to track the different motion states of the needle and probe. Thus, the overall calibration of the needle and probe did not utilize an external tracker and phantom. The imaging quality, however, was inadequate due to manual scanning of the US probes, which may cause a low robustness assessment.

VI. Conclusion and Future Work

This paper presents a calibration approach based biplane TRUS probe using dual-arm robotic needle insertion system with multi-DOF end-effectors. The proposed method utilized the biplane to track the probe and needle positions when translated and rotated, eliminating the requirement for an additional camera or position sensor. As a result, the dual-arm, multi-DOF robotic needle insertion system was calibrated with a high calibration accuracy of 0.80±0.23 mm. Furthermore, we first determined the kinematic parameters of the probe and needle, which were divided into three parts: initial, translational, and rotational parameters. After that, these parameters were calibrated to achieve different motion states for the needle and probe. Finally, several experiments have been conducted with the newly developed TRUS-guided

dual-arm robotic needle insertion system. The experimental results demonstrate the feasibility of the proposed method.

In the future, we will study the acquisition of ultrasonic images using a force feedback control ultrasonic probe. This will enable us to reduce the error caused by soft tissue deformation during needle insertion and improve needle insertion accuracy in soft tissue.

References

[1] Burgner-Kahrs, J., Rucker, D.C. and Choset, H., 2015. Continuum robots for medical applications: A survey. IEEE Transactions on Robotics, 31(6), pp.1261-1280.

[2] van Amsterdam, B., Clarkson, M.J. and Stoyanov, D., 2021. Gesture recognition in robotic surgery: a review. IEEE Transactions on Biomedical Engineering, 68(6).

[3] Lim, S., Jun, C., Chang, D., Petrisor, D., Han, M. and Stoianovici, D., 2019. Robotic transrectal ultrasound guided prostate biopsy. IEEE transactions on biomedical engineering, 66(9), pp.2527-2537.

[4] Brown, A.M., Elbuluk, O., Mertan, F., Sankineni, S., Margolis, D.J., Wood, B.J., Pinto, P.A., Choyke, P.L. and Turkbey, B., 2015. Recent advances in image-guided targeted prostate biopsy. Abdominal imaging, 40(6), pp.1788-1799.

[5] Chen, Y., Xu, S., Squires, A., Seifabadi, R., Turkbey, I.B., Pinto, P.A., Choyke, P., Wood, B. and Tse, Z.T.H., 2017. MRI-guided robotically assisted focal laser ablation of the prostate using canine cadavers. IEEE Transactions on Biomedical Engineering, 65(7), pp.1434-1442.

[6] Bader, K.B., Hendley, S.A. and Bollen, V., 2020. Assessment of collaborative robot (Cobot)-assisted histotripsy for venous clot ablation. IEEE Transactions on Biomedical Engineering, 68(4), pp.1220-1228.

[7] Wei, Z., Wan, G., Gardi, L., Mills, G., Downey, D. and Fenster, A., 2004. Robot?assisted 3D?TRUS guided prostate brachytherapy: System integration and validation. Medical physics, 31(3), pp.539-548.

[8] Su, H., Shang, W., Cole, G., Li, G., Harrington, K., Camilo, A., Tokuda, J., Tempany, C.M., Hata, N. and Fischer, G.S., 2014. Piezoelectrically actuated robotic system for MRI-guided prostate percutaneous therapy. IEEE/ASME transactions on mechatronics, 20(4), pp.1920-1932.

[9] Kojcev, R., Fuerst, B., Zettinig, O., Fotouhi, J., Lee, S.C., Frisch, B., Taylor, R., Sinibaldi, E. and Navab, N., 2016. Dual-robot ultrasound-guided needle placement: closing the planning-imaging-action loop. International journal of computer assisted radiology and surgery, 11(6), pp.1173-1181.

[10] Mohareri, O., Ramezani, M., Adebar, T.K., Abolmaesumi, P. and Salcudean, S.E., 2013. Automatic localization of the da Vinci surgical instrument tips in 3-D transrectal ultrasound. IEEE Transactions on Biomedical Engineering, 60(9), pp.2663-2672.

[11] Ottacher, D., Chan, A., Parent, E. and Lou, E., 2020. Positional and orientational accuracy of 3-D ultrasound navigation system on vertebral phantom study. IEEE Transactions on Instrumentation and Measurement, 69(9), pp.6412-6419.

[12] Jeong, W., Kumar, R. and Menon, M., 2016. Past, present and future of urological robotic surgery. Investigative and clinical urology, 57(2), pp.75-83.

[13] Jiang, J.G., Zuo, H., Zhang, Y.D., Huang, Z.Y., Guo, X.W. and Xu, Y., 2020. Design and Experiment of Assistive Mechanism for Adjustment of Transrectal Ultrasound Probe. Applied Bionics and Biomechanics, 2020.

[14] Xiong, J., Xu, C., Ibrahim, K., Deng, H. and Xia, Z., 2021. A mechanism-image fusion approach to calibration of an ultrasound-guided dual-arm robotic brachytherapy system. IEEE/ASME Transactions on Mechatronics, 26(6), pp.3211-3220.

[15] Mercier, L., Lang, T., Lindseth, F. and Collins, D.L., 2005. A review of calibration techniques for freehand 3-D ultrasound systems. Ultrasound in medicine and biology, 31(4), pp.449-471.

[16] Prager, R.W., Ijaz, U.Z., Gee, A.H. and Treece, G.M., 2010. Three-dimensional ultrasound imaging. Proceedings of the Institution of Mechanical Engineers, Part H: Journal of Engineering in Medicine, 224(2), pp.193-223.

[17] Zhao, Y.M., Lin, Y., Xi, F. and Guo, S., 2014. Calibration-based iterative learning control for path tracking of industrial robots. IEEE Transactions on industrial electronics, 62(5), pp.2921-2929.

[18] Wu, L., Wang, J., Qi, L., Wu, K., Ren, H. and Meng, M.Q.H., 2016. Simultaneous Hand?Eye, Tool?Flange, and Robot?Robot Calibration for Comanipulation by Solving the $\mathbf{AXB} = \mathbf{YCZ}$ Problem. IEEE TRansactions on robotics, 32(2), pp.413-428.

[19] Fu, Z., Pan, J., Spyrakos-Papastavridis, E., Chen, X. and Li, M., 2020. A dual quaternion-based approach for coordinate calibration of dual robots in collaborative motion. IEEE Robotics and Automation Letters, 5(3), pp.4086-4093.

[20] Boctor, E., Viswanathan, A., Choti, M., Taylor, R.H., Fichtinger, G. and Hager, G., 2004, April. A novel closed form solution for ultrasound calibration. In 2004 2nd IEEE International Symposium on Biomedical Imaging: Nano to Macro (IEEE Cat No. 04EX821), pp. 527-530.

[21] Shen, J., Zemiti, N., Dillenseger, J.L. and Poignet, P., 2018, July. Fast and simple automatic 3D ultrasound probe calibration based on 3D printed phantom and an untracked marker. In 2018 40th Annual International Conference of the IEEE Engineering in Medicine and Biology Society (EMBC) pp. 878-882.

[22] Wang, J., Wu, L., Meng, M.Q.H. and Ren, H., 2014, September. Towards simultaneous coordinate calibrations for cooperative multiple robots. In 2014 IEEE/RSJ International Conference on Intelligent Robots and Systems pp. 410-415.

[23] Ma, Q., Goh, Z., Ruan, S. and Chirikjian, G.S., 2018. Probabilistic approaches to the AXB= YCZ AXB = YCZ calibration problem in multi-robot systems. Autonomous Robots, 42(7), pp.1497-1520.

[24] Carbajal, G., Lasso, A., G mez, . and Fichtinger, G., 2013. Improving N-wire phantom-based freehand ultrasound calibration. International journal of computer assisted radiology and surgery, 8(6), pp.1063-1072.

[25] Kim, C., Chang, D., Petrisor, D., Chirikjian, G., Han, M. and Stoianovici, D., 2013. Ultrasound probe and needle-guide calibration for robotic ultrasound scanning and needle targeting. IEEE Transactions on Biomedical Engineering, 60(6), pp.1728-1734.

[26] Najafi, M., Afsham, N., Abolmaesumi, P. and Rohling, R., 2014. A closed-form differential formulation for ultrasound spatial calibration: multi-wedge phantom. Ultrasound in medicine and biology, 40(9), pp.2231-2243.

[27] Shen, C., Lyu, L., Wang, G. and Wu, J., 2019. A method for ultrasound probe calibration based on arbitrary wire phantom. Cogent Engineering, 6(1), p.1592739.

[28] Zhang, H.K., Cheng, A., Kim, Y., Ma, Q., Chirikjian, G.S. and Boctor, E.M., 2018. Phantom with multiple active points for ultrasound calibration. Journal of Medical Imaging, 5(4), p.045001.

[29] Shiu, Y.C. and Ahmad, S., 1987. Calibration of wrist-mounted robotic sensors by solving homogeneous transform equations of the form AX= XB.

[30] Snow, K. and Schaffrin, B., 2016. Line fitting in Euclidean 3D space. Studia geophysica et geodaetica, 60(2), pp.210-227.

[31] K sa, I., 1976. A circle fitting procedure and its error analysis. IEEE Transactions on instrumentation and measurement, (1), pp.8-14.

[32] Stoianovici, D., Kim, C., Petrisor, D., Jun, C., Lim, S., Ball, M.W., Ross, A., Macura, K.J. and Allaf, M.E., 2016. MR safe robot, FDA clearance, safety and feasibility of prostate biopsy clinical trial. IEEE/ASME Transactions on Mechatronics, 22(1), pp.115-126.